applied sciences

MDPI

Article

Experimental Characterization and Finite Element Modeling of the Effects of 3D Bioplotting Process Parameters on Structural and Tensile Properties of Polycaprolactone (PCL) Scaffolds

Lokesh Karthik Narayanan[1], and Rohan A. Shirwaiker [2,3,4,5]*

[1] Department of Industrial and Manufacturing Engineering, North Dakota State University, Fargo, ND 58103; lokesh.narayanan@ndsu.edu
[2] Edward P. Fitts Department of Industrial and Systems Engineering, North Carolina State University, Raleigh, NC 27695; rashirwaiker@ncsu.edu
[3] Center for Additive Manufacturing and Logistics, North Carolina State University, Raleigh, NC 27695;
[4] Comparative Medicine Institute, North Carolina State University, Raleigh, NC 27695;
[5] Joint Department of Biomedical Engineering, University of North Carolina - North Carolina State University, Raleigh, NC 27695; rashirwaiker@ncsu.edu
* Correspondence: rashirwaiker@ncsu.edu;

Received: date; Accepted: date; Published: date

Abstract: In this study we have characterized the process-structure interactions in melt extrusion-based 3D Bioplotting of polycaprolactone (PCL), and developed predictive models to enable the efficient design and processing of scaffolds for tissue engineering applications. First, the effects of pneumatic extrusion pressure (0.3, 0.4, 0.5, 0.6 N/mm^2), nozzle speed (0.1, 0.4, 1.0, 1.4 mm/s), strand lay orientation (0°, 45°, 90°, 135°) and strand length (10, 20, 30 mm) on the strand width were investigated and a regression model was developed to map strand width to the two significant parameters (extrusion pressure and nozzle speed; $p < 0.05$). Then, proliferation of NIH/3T3 fibroblast cells in scaffolds with two different stand widths fabricated with different combinations of the two significant parameters was assessed over 7 days which showed that the strand width had a significant effect on proliferation ($p < 0.05$). The effect of strand lay orientations (0° and 90°) on tensile properties of non-porous PCL specimens was determined and were found to be significantly higher for specimens with 0° lay orientation ($p < 0.05$). Finally, this data was used to develop and experimentally validate a finite element model for a porous PCL specimen with 1:1 ratio of inter-strand spacing to strand width.

Keywords: 3D Bioplotting, scaffolds, finite element analysis, tensile strength, PCL

---

1. Introduction

Tissue engineering and regenerative medicine strategies focus on the creation of biological substitutes for clinical therapeutics and diagnostics, drug screening, and disease modelling through the application of multidisciplinary engineering and life sciences principles [1,2]. One widely used strategy relies on the use of three-dimensional (3D) substrates, referred to as scaffolds, to house cells throughout their porous micro-architecture and serve as a template for the generation of extracellular matrix (ECM). In addition to providing the appropriate physiological environments for cells to proliferate and secrete ECM, scaffolds must also possess mechanical and structural properties comparable to those of native tissues.

Scaffolds have been fabricated using a variety of biomaterials ranging from natural materials such as collagen, chitosan, hyaluronic acid, alginate, and silk fibroin to synthetic polymers including polycaprolactone (PCL), polylactic acid, polyglycolic acid, and polyurethanes [3,4]. PCL, a biodegradable semi-crystalline linear aliphatic polyester that is already being used in FDA-approved or cleared medical devices, has been one of the most commonly investigated scaffold biomaterial. A simple Google Scholar search using the keyword "PCL scaffolds" showed over 8775 results. PCL is miscible with a large range of other polymers and has a relatively slow biodegradation rate as well as a relatively low melting point. The latter property especially makes it suitable for several fabrication processes. Scaffold fabrication can be classified into traditional processes (e.g., solvent casting/particulate leaching, freeze-drying, phase inversion, electrospinning) and additive manufacturing (AM) processes (e.g., selective laser sintering (SLS) [5,6] , fused deposition modeling (FDM) [7,8] , 3D Bioplotting (3DB) [9–11], stereolithography [12,13]). In recent years, AM processes have become more prominent because they offer better control over scaffold macro- and micro-architecture, better reproducibility, and improved processing efficiency when compared to traditional processes. In general, AM processes offer greater flexibility to reproduce complex anatomical geometries allowing the creation of patient-specific scaffolds. 3DB is one commonly used pneumatic extrusion-based AM process for scaffold fabrication. It allows the processing of biomaterials in their molten or solution forms, thereby enabling the fabrication of acellular polymer scaffolds as well as cell-encapsulated hydrogel constructs [14–16]. Furthermore, multiple materials can be printed within the same build, thereby providing the ability to create hybrid constructs with a multi-material framework with or without encapsulated cells.

Strands are the fundamental building blocks of bioplotted scaffolds; scaffolds are built layer-by-layer, and strands constitute each layer. The porous micro-architecture of a scaffold is governed by the strand dimensions, strand lay orientation, and inter-strand spacing. These parameters affect the scaffold mechanical properties as well as the distribution of cells and nutrient exchange once cells are cultured onto them. In 3DB, since strands are created by extruding the melt through the nozzle of a moving dispensing head, process parameters such as the nozzle internal diameter, extrusion temperature, extrusion pressure, and nozzle speed affect the strand width. The strand width is sensitive to changes in these process parameters due to the non-Newtonian flow of the melt and the shear stresses as it is pressurized through the nozzle [17]. The mechanical properties are also affected by the process parameters due to melt deformation at the nozzle. There is strong evidence that the properties of polymers processed using extrusion-based AM processes differ significantly in comparison to their unprocessed or injection molded forms [18,19]. From a process engineering perspective, it is important to study the relationships between these process parameters, strand dimensions, and resulting mechanical properties of the scaffold. Understanding these relationships can enable the engineering of application-specific scaffolds with greater precision and reproducibility.

Several studies have modeled the effects of extrusion-based AM parameters on the quality of fabricated structures. For example, Anitha et al. mapped the effects of layer height, strand width and nozzle speed on the surface roughness of the FDM-printed specimens [20]. Górski et al. modeled the effects of lay orientation, layer height, and layer filling strategy on the mechanical strength, surface quality, accuracy and manufacturing time of FDM-printed acrylonitrile butadiene styrene structures [21]. In terms of additively manufactured PCL scaffolds, Eshraghi and Das reported on the mechanical properties of SLS-printed PCL with different strand lay orientations and micro-architectures [22]. Liu et al. determined the effects of screw rotational speed and melting temperature on tensile strength and crystalline structure of extruded PCL filaments [23]. Sheshadri and Shirwaiker demonstrated the effects of two 3DB parameters, extrusion temperature and nozzle inner diameter, on the strand width and compression modulus of PCL scaffolds [11]. However, for 3DB process the effects of extrusion pressure, nozzle speed, and strand orientation on strand width and mechanical properties of extruded PCL have not been characterized in literature. Furthermore, computational models to estimate the mechanical properties are not available in literature either.

This study aims to contribute to our overall understanding of the process-structure interactions in melt extrusion-based 3DB of PCL. The focus is on experimental characterization and subsequent statistical and finite element (FE) modeling of the effects of process parameters on structural and tensile properties of bioplotted PCL. The study was conducted in three interconnected phases (Figure 1). In Phase-1, the relationships between strand width and extrusion pressure, nozzle speed, lay orientation, and strand length were characterized. A regression model to estimate the strand width based on critical process parameters was developed and validated. To test the validity of hypothesis that the strand width has an effect on the cell proliferation within a scaffold, two sets of porous scaffolds (Ø 20 × 2 mm, 0°/90° strand lay orientation) with contrasting strand widths resulting from extreme combinations of extrusion pressure and nozzle speed within the established design space were tested with NIH/3T3 fibroblast cells over 7 days in culture. Once the process-structure characteristics were understood, in Phase-2, the effect of stand lay orientation on tensile properties of bulk bioplotted PCL structures was determined. In the context of this study, bulk refers to specimen bioplotted with non-porous gage sections, i.e., adjacent strands printed with no inter-strand spacing. These bulk tensile properties were critical in creating the FE model. Finally in Phase 3, using the strand width data from Phase-1 and tensile testing results from Phase-2, a FE model was developed and validated to computationally estimate the tensile strength of 3D bioplotted porous PCL structures.

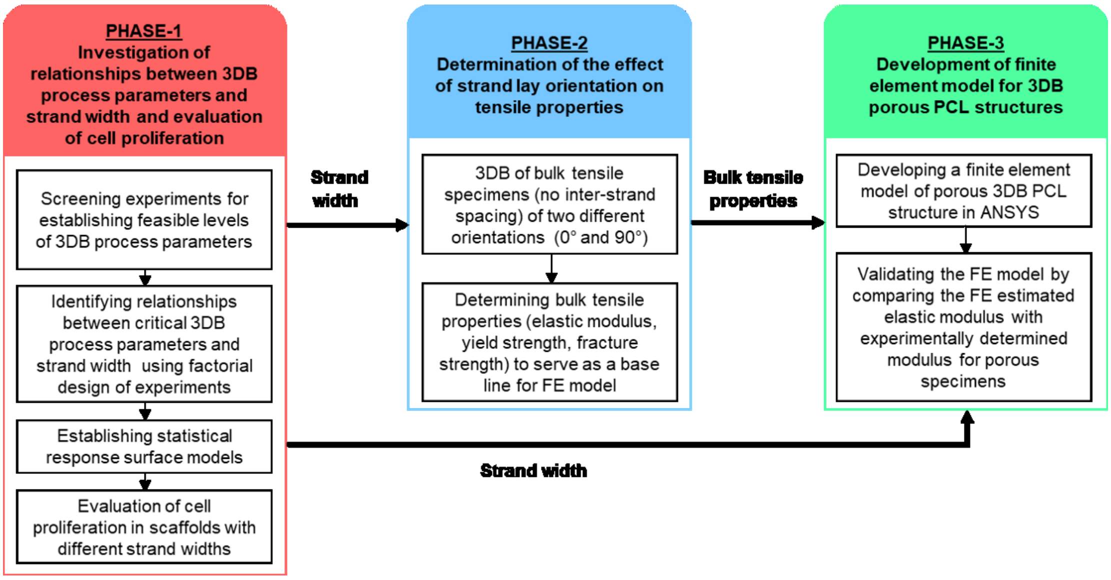

Figure 1. Overview of the methodology presented in this paper

2. Materials and Methods

2.1 Phase-1: Investigating relationships between 3D Bioplotting parameters, strand width, and cell proliferation

2.1.1 3D Bioplotting parameter screening

Pneumatic extrusion pressure, nozzle speed (both process-specific), lay orientation, and strand length (both geometry-specific) were the 3DB parameters of interest, and PCL (Ø 3 mm pellets, Mw 43,000 Da; Polysciences Inc., Warrington, PA) was the material being investigated. All bioplotting described in this paper was performed using a high-temperature printhead with a Ø 0.3 mm (inner diameter) nozzle on the 3D-Bioplotter (Manufacturer Series, EnvisionTEC GmbH, Gladbeck, Germany). The printhead was set to 120 °C, and the PCL pellets were preheated for 30 mins before initiating the print cycle. Prior to the factorial design of experiments (DoE), screening experiments were performed to determine the feasible levels for the two process-specific parameters. The maximum extrusion pressure and minimum nozzle speed were governed by the machine and operational capabilities. The minimum level of pressure and maximum level of speed were determined using a screening algorithm wherein combinations of these two parameters were identified at which the material could be feasibly extruded without any visual defects (discontinuous/intermittent deposition, abrupt thinning/thickening) while bioplotting three types of bioplotted structures – 1) individual 30 mm long strands, 2) layers with alternating 0°/90° strand lay orientation and 1:1 ratio of strand width to inter-strand spacing, and 3) scaffolds of 5 mm thickness with 0°/90° strand lay orientation and 1:1 ratio of strand width to inter-strand spacing.

2.1.2 Factorial design of experiments

A mixed level DoE was formulated with the four input factors – extrusion pressure, nozzle speed, lay orientation and strand length – and strand width as the response variable (Table 1). The nozzle inner diameter and extrusion temperature were kept constant throughout the study (0.3 mm and 120°C, respectively). Three replicates were bioplotted for each combination of speed and pressure as per the pattern shown in Table 1. This pattern incorporated the two geometry-specific factors (strand lay orientation, strand length). The strand lay orientation and strand length levels were chosen to represent commonly used values in literature [24]. Previously published 3DB and strand width measurement protocols were followed [11]. For each strand, the width was measured at 3 locations (ends and midpoint).

Table 1. Phase 1 DoE factors, levels and print pattern

Factors	**Levels**	**Print pattern (all dimensions in mm)**
Extrusion pressure	0.3, 0.4, 0.5, 0.6 N/mm^2	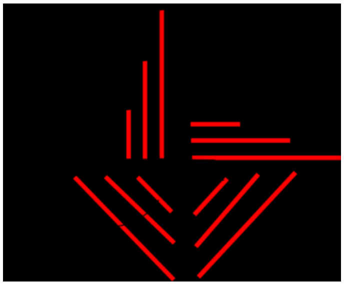
Nozzle speed	0.1, 0.4, 1.0, 1.4 mm/s	
Lay orientation	0°, 45°, 90°, 135°	
Strand length	10, 20, 30 mm	

2.1.3 Statistical analyses and model validation

The effects of the four factors and their interactions on the strand width were assessed using analysis of variance (ANOVA) ($\alpha = 0.05$). A predictive equation was developed to estimate the strand width based on statistically significant factors by fitting the best least square regression model. All statistical analyses were performed in JMP Pro (SAS, Cary, NC). To validate the predictive model, strands (n = 3) were bioplotted using a different set of process parameters within the design space (extrusion pressure of 0.35 N/mm^2 and nozzle speed of 0.9 mm/s), and the experimental strand width was compared to its model estimate.

2.1.4 3D Bioplotting of porous scaffolds for evaluating cellular activity

The base CAD model for the scaffolds was created in SolidWorks (Dassault Systems, SolidWorks Corporation, Waltham, MA) as a cylinder (Ø 20 × 2 mm). The STL file of the model was sliced into layers of 0.24 mm thickness and positioned on the 3D-Bioplotter stage using BioplotterRP software (EnvisionTEC GmbH). The layer height of 0.24 mm corresponded to the recommended thickness equal to 80% of nozzle diameter (0.3 mm). The file was then preprocessed in VisualMachines software (EnvisionTEC GmbH) to assign an alternating 0°/90° strand lay down pattern and set the processing parameters. Two scaffold designs with contrasting fiber widths were fabricated with extrusion pressure-nozzle speed combinations of 0.3 N/mm^2 – 0.1 mm/s and 0.6 N/mm^2 – 1.4 mm/s, henceforth referred to as 3DB1 and 3DB2 designs, respectively. These pressure-speed combinations were chosen based on the design space established as per section 2.1.1. The inter-axial strand separation was set to 1.1 mm and 0.3 mm for 3DB1 and 3DB2, respectively. The interstrand spacing corresponded to the average strand width recorded for the chosen pressure-speed combination as recorded in section 2.1.2, thereby creating a porous architecture with 1:1 strand width to inter-strand spacing ratio for both, 3DB1 and 3DB2 designs. PCL being hydrophobic in nature, all scaffolds were subjected to alkaline hydrolysis surface modification to enhance their hydrophilicity and improve cellular adhesion during the cell culture. Scaffolds were submerged in a solution of 2.5M NaOH for 30 minutes at 37°C under continuous agitation. After this treatment, scaffolds were rinsed thoroughly with DI water, sterilized for 30 minutes in a bath of 70% ethanol, rinsed thoroughly with phosphate buffer solution (PBS) (Thermo Fisher Scientific, Waltham, MA), and finally, dried within a biosafety cabinet prior to cell seeding.

2.1.5 Cell expansion and seeding of scaffolds

NIH/3T3 fibroblasts (CRL-1658™, ATCC, VA) were cultured with 90 % v/v minimum essential medium without L-glutamine (MilliporeSigma, Burlington, MA) and 10 % v/v fetal bovine serum (Thermo Fisher Scientific) in a in T-75 flasks (Nunc™ Easy Flask™, Thermo Fisher Scientific) at 37°C (5% CO_2) with media changes on alternate days until 90 % confluency. The cells were harvested by adding 3 mL of TrypLE™ Select Enzyme (Thermo Fisher Scientific) after two washes with 5 mL of PBS. The dissociated cell suspension was neutralized with media and centrifuged to obtain cell pellets. The pellets were suspended in 1 mL of the culture medium at a concentration of $1x10^6$ cells/mL.

Four scaffolds of each design were used during experiments – three scaffolds (n = 3) were seeded and used as treatment samples, and one acellular scaffold served as control for aB assay. Sterile scaffolds were seeded in a twelve-well culture plate (Thermo Fisher Scientific) in two steps. First, 1 mL of cell suspension was added onto each scaffold. The scaffolds were incubated (37°C, 5% CO_2) for 2 hours, and an additional 2 mL of media was added to each. After 24 hours of incubation, the scaffolds were flipped and the process was repeated to seed the other side with another 1×10^6 cells, bringing the total to 2×10^6 cells. After 24 hours of incubation, the scaffolds were transferred to a six-well plate (Thermo Fisher Scientific) and cultured in 4 mL of media over 7 days, with media changes performed every 24 hours.

2.1.6 Cell proliferation assays

The alamarBlue (aB) colorimetric reduction assay (Thermo Fisher Scientific) was performed on the scaffolds on days 1, 3, 5 and 7 of culture to asses cell proliferation. During media changes, fresh media containing 10% v/v of the aB reagent was added and the scaffolds were incubated for 4 hours. Post incubation, three 1 mL samples were pipetted from each scaffold into a twenty four-well plate (Thermo Fisher Scientific), and the absorbance was measured using a microplate reader (Tecan, Männedorf, Switzerland) with excitation and emission wavelengths of 570 nm and 600 nm, respectively. The absorbance data was converted to and is reported as % aB reduction [25]. A two-way ANOVA was performed on % aB reduction of the scaffolds with scaffold design (3DB1 and 3DB2) and day of aB measurement (1, 3, 5, 7) as factors ($\alpha = 0.05$). Following the ANOVA, Tukey's HSD post hoc tests were performed with scaffold designs as a factor on individual days of measurement ($\alpha = 0.05$). Viable cells that attached to the scaffold strands were visualized using LIVE/DEAD® staining (Life Technologies, Carlsbad, CA) following aB measurement on Day 7. Each scaffold was incubated in 1 mL PBS containing 0.5 µl calcein AM and 2 µl EthD-I for 10 minutes and imaged using a fluorescence microscope (Revolve, Echo, San Diego, CA).

2.2 Phase-2: Determining the effect of strand lay orientation on tensile properties of bioplotted PCL

2.2.1 3D Bioplotting of bulk PCL tensile specimens

The tensile test specimens were designed as per ASTM D638 (non-rigid plastics, type IV) with two different strand lay orientations [26] (Figure 2). In the 0° configuration, all strands were oriented along the direction of tensile loading. In the 90° configuration, all strands were oriented perpendicular to the direction of tensile loading. These two strand lay orientations were chosen due to their prevalence in tissue engineering scaffolds literature [9,25,27,28]. Three bulk samples were bioplotted for each configuration using a Ø 0.3 mm nozzle at 120°C with an extrusion pressure of 0.5 N/mm^2, a nozzle speed of 1.4 mm/s and with a layer height of 0.26 mm. It should be noted that experimentally characterizing the bulk tensile properties across all combinations of bioplotting parameters was not feasible due to the time and resource-intensiveness associated with fabricating the bulk PCL specimens. Hence, the aforementioned representative set of bioplotting parameters was chosen from within the Phase-1 design space (Table 1) as it has been successfully used in a previous study [25].

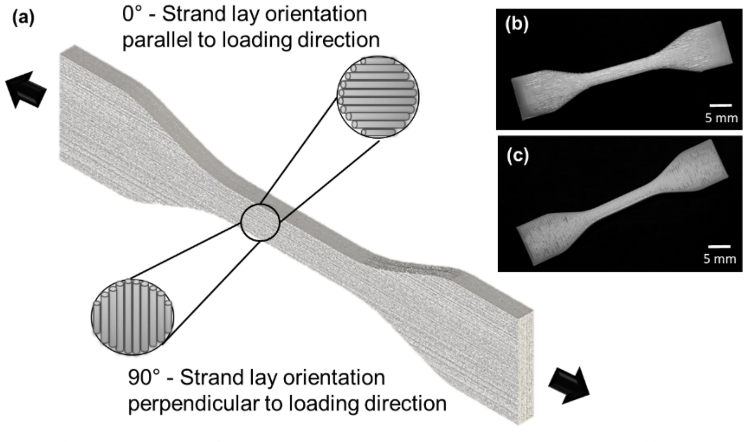

Figure 2. (a) Tensile specimen design as per ASTM D638 Type IV (all dimensions in mm), Representative images of 3D Bioplotted bulk specimen of **(b)** 0° configuration and **(c)** 90° configuration

2.2.2 Tensile testing

The specimens (n = 3 per lay orientation) were tested in tension on an ATS 1605C universal tester (Applied Test Systems, Butler, PA) at a displacement of 50 mm/min. Each specimen was loaded to failure, and the load versus displacement curves were used to compute the corresponding engineering stress versus strain plots. The slope of the linear region of the plot up to the yield point is reported as the elastic modulus. The yield strength is reported as the 0.2% strain offset of maximum stress endured by the specimen. The stress endured during fracture is reported as the fracture strength.

2.2.3 Statistical analysis

Statistically significant differences in elastic modulus, yield strength and fracture strength between 0° and 90° configurations were determined using Student's t-test ($p < 0.05$) in JMP Pro.

2.3 Phase-3: Developing and validating finite element model for bioplotted PCL

A CAD model was created to reflect the tensile specimen gage section (33 x 6 x 3.2mm). The model contained 13 layers with alternating 0/90° strand lay orientation. The strand width and inter-strand spacing were both set at 330 μm, and the inter-layer strand overlap was set to 70 μm to reflect the average dimensions of the experimental specimens. FE analyses were performed in ANSYS (Ansys Inc, Canonsburg, PA) using the model input parameters presented in Table 2. The density of bioplotted PCL was computed based on measured volume and mass of PCL strands (n = 12) of 30 mm length bioplotted using a Ø 0.3 mm nozzle at 120°C with an extrusion pressure of 0.5 N/mm^2 and nozzle speed of 1.4 mm/s. The Poisson's ratio was assumed to be 0.3 based on literature [22,29]. Given the alternating 0/90° strand lay orientation in the specimen, the elastic modulus and yield strength were assigned to be the average of those respective measures determined from the tensile testing of 0° and 90° configurations in Phase-2.

Table 2 FE model parameters

Model type	**Static structure**
Material category	Isotropic elasticity
Density (g/mm^3)	3.16×10^{-4}
Elastic modulus (N/mm^2)	58.14
Poisson's ratio	0.3
Yield strength (N/mm^2)	12.60

The model was set up as a static structure and meshed using curvature controlled triangular elements with a minimum edge length of 3 μm. A displacement step function corresponding to experimental strain rate of 50 mm/min was applied on one end of the specimen while the other end was constrained using fixed support with the interface set as bonded material. The model was then solved to estimate equivalent stress (von Mises). Using the probe tool, the reaction force and effective strain were determined at the fixed end. The effective elastic modulus of the model was determined based on the reaction force, effective strain and effective area using Equation 1. The effective area was assumed to be the sum of cross-sectional area of the 0° oriented strands, since only these strands were aligned along the direction of loading.

$$Effective\ \ elastic\ \ modulus = \frac{Reaction\ \ force}{Effective\ \ area \times\ Effective\ \ strain} \tag{1}$$

For experimental validation, PCL tensile testing specimens (n = 3) with geometry matching the FE model (strand width = inter-strand spacing = 330 μm, 13 layers, 0°/90° strand lay orientation) were bioplotted using a Ø 0.3 mm nozzle at 120°C with a pressure of 0.5 N/mm^2 and nozzle speed of 1.4 mm/s. Tensile testing was performed using the previously described procedure. The effective area for stress calculation was computed based on the image analysis of the cross-section of the bioplotted porous specimen gage. The average experimental elastic modulus was compared to the effective elastic modulus estimate from the FE model.

3. Results

3.1 Phase-1: Relationships between 3D-Bioplotting parameters, strand width, and cell proliferation

ANOVA results and post hoc test show that extrusion pressure, nozzle speed, and their interaction had a statistically significant effect ($p < 0.001$) on the strand width. The strand widths (mean ± standard deviation) for the 16 combinations of extrusion pressure and nozzle speed are presented in Table S1 and the corresponding response surface plot is presented in Figure 3. A general trend of decrease in strand width with increasing nozzle speed and decreasing extrusion pressure was observed.

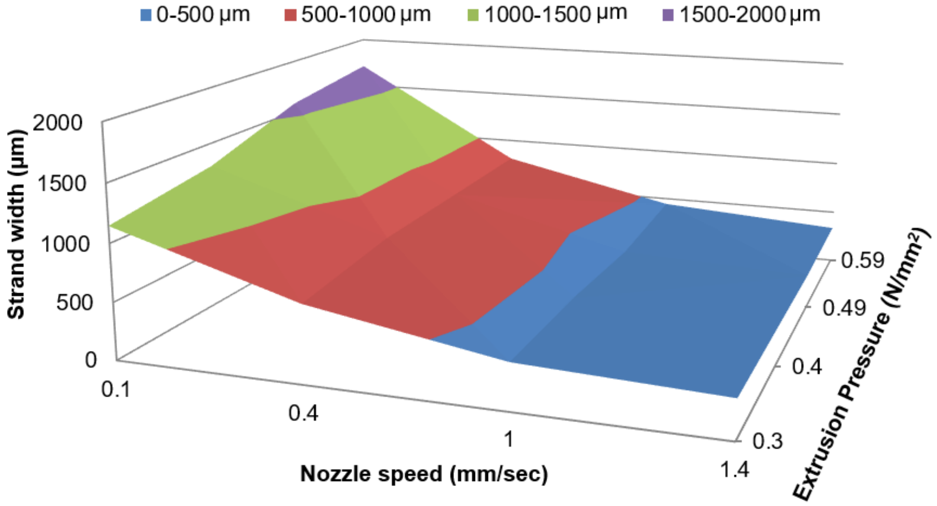

Figure 3. A Response surface plot of strand width (µm) for combinations of different levels of extrusion pressure and nozzle speed.

A total of ten regression models ranging from squared to logarithmic were fitted to the data, and the model in Equation 2 provided the best R-squared value of 0.9046. In Equation 2, extrusion pressure is given in N/mm^2, nozzle speed in mm/s, and the strand width is estimated in µm. From a validation perspective, the difference between the strand width estimate from this model (428.02 µm) and the average experimental strand width (412.34 µm) was 3.8%, which indicates good model fidelity.

$$Strand\ width = 368.17 + 132.70 * extrusion\ pressure - 368.45 * Log(nozzle\ speed) - 798.53 * [(extrusion\ pressure - 0.44) * Log(nozzle\ speed)] \tag{2}$$

Results of %aB reduction for the 3DB1 and 3DB2 scaffold designs are presented in Figure 4(a). The %aB reduction of both designs increased over time in culture, signifying an increase in cell proliferation. Overall, the % aB reduction for the 3DB2 scaffolds was higher than the 3DB1 scaffolds. Results from the two-way ANOVA show that both the scaffold design and the days in culture had a significant effect on % aB reduction ($p < 0.05$). Tukey's HSD post hoc results show that the differences in % aB reduction between scaffold designs (pairwise comparisons) were significant on days 1, 3, and 5, but not on day 7. The Live/Dead® images show that the viable cells (green dots) adhered to the strands of both scaffold designs (Figure 4(b) and (c)). Dead cells, which would have manifested as red dots, were not observed, indicating cell viability approximating 100% in both designs.

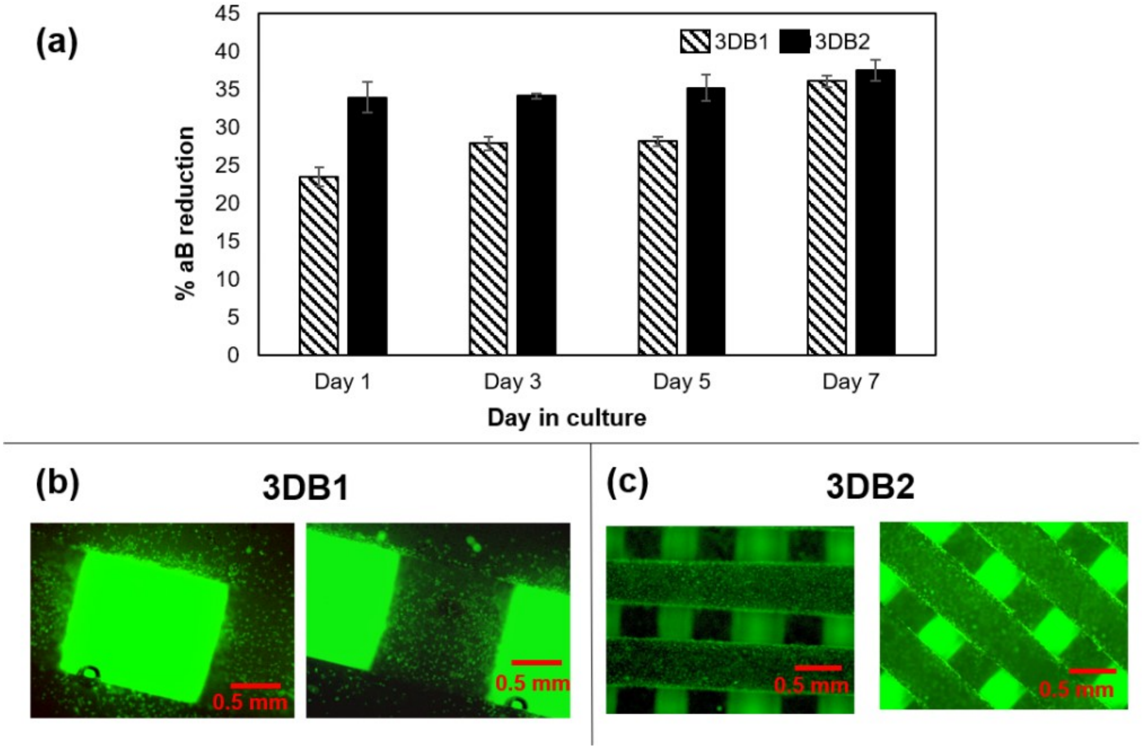

Figure 4. (a) % aB reduction of 3DB1 and 3DB2 scaffolds over 7 days. Error bars denote standard deviation (n = 3). (b) Representative Live/Dead image of 3DB1 and 3DB2 scaffolds, respectively, seeded with 2 x10^6 NIH/3T3 cells on Day 7. Live cells that attached to the strands (darker regions) are stained green (dots). The square regions irradiating green fluorescence in between the strands are empty pores.

3.2 Phase-2: Effect of strand lay orientation on tensile properties of bioplotted PCL

Stress versus strain plots for the 0° and 90° strand lay orientation configurations are presented in Figure 5. The elastic modulus, yield strength, and fracture strength determined from these plots are also specified. The plots show that as the specimens of both configurations started to yield, the stress values decreased, but the time to fracture was shorter for the 90° configuration. For the 0° configuration, the cyclic stress undulations after a strain of 1 can be attributed to the spasmodic plastic deformation of individual strands in the specimens. This phenomenon was not observed in the 90° configuration. The trends observed for strain values less than 1 are similar to tensile characteristics observed in viscous polymers [30–32]. Student t-test results indicate that for each of the three tensile measures, the differences between specimens of 0° and 90° configurations were statistically significantly different ($p < 0.05$), implying that the strand lay orientation had a significant effect on tensile properties of bioplotted PCL. The 0° configuration had higher values for all three tensile measures.

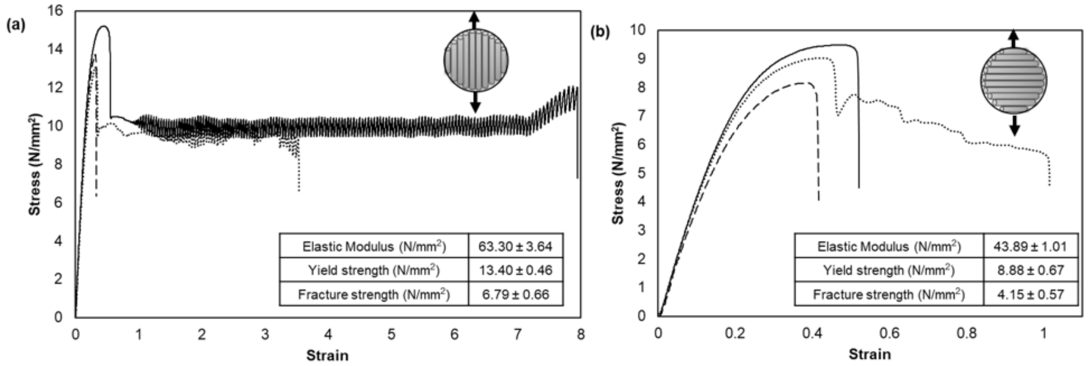

Elastic Modulus (N/mm²)	63.30 ± 3.64
Yield strength (N/mm²)	13.40 ± 0.46
Fracture strength (N/mm²)	6.79 ± 0.66

Elastic Modulus (N/mm²)	43.89 ± 1.01
Yield strength (N/mm²)	8.88 ± 0.67
Fracture strength (N/mm²)	4.15 ± 0.57

Figure 5. Plots of stress versus strain for three bulk specimens of **(a)** 0° configuration and **(b)** 90° configuration after Phase-2 tensile testing, represented by lines with different types of line style.

3.3 Phase-3: Finite element modeling and validation

The meshed FE model of the tensile specimen gage with strand width to inter-strand spacing ratio of 1:1 contained 2,045,737 triangular elements and 3,424,882 nodes. The stress distribution in the model is presented in Figure 6. The average stress in the 0° and 90° oriented strands was 16.57 N/mm² and 1.36 N/mm² respectively. The higher stress in 0° oriented strands is on account of them being aligned along the direction of loading. The average reaction force determined by averaging the force on all the nodes at the fixed end, was 113 N corresponding to a strain of 0.59 acting across a cross-sectional area of 5.09 mm², resulting in effective elastic modulus of 37.51 N/mm² (Equation 1).

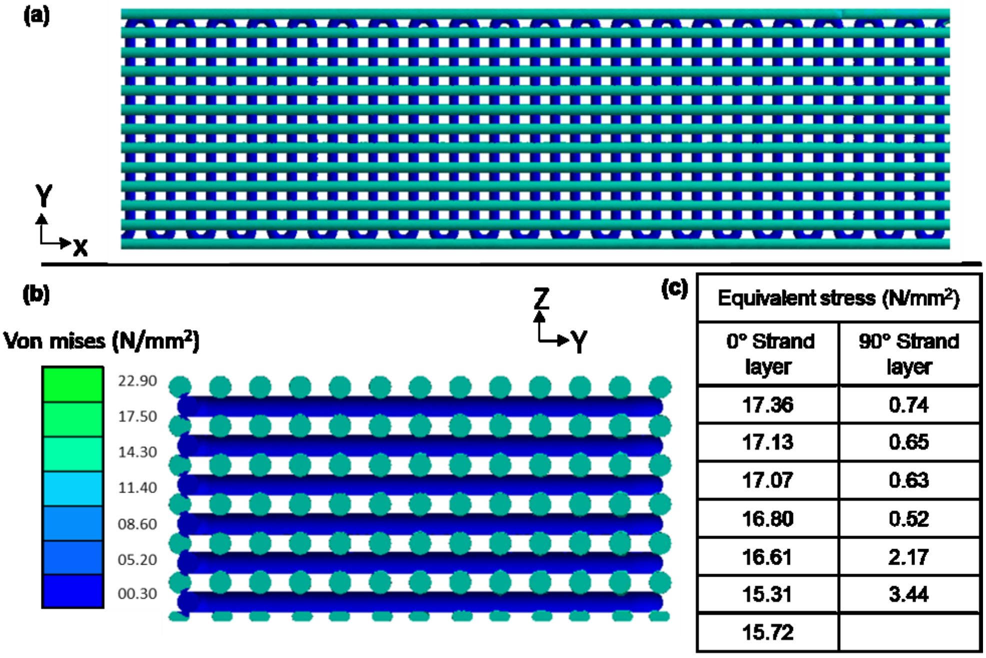

Equivalent stress (N/mm²)	
0° Strand layer	90° Strand layer
17.36	0.74
17.13	0.65
17.07	0.63
16.80	0.52
16.61	2.17
15.31	3.44
15.72	

Figure 6. FE estimated equivalent (Von Mises) stress at a maximum strain of 0.59: **(a)** Stress distribution along X-Y plane, and **(b)** Stress distribution across the cross-section of the model, and average stress across each layer oriented along or perpendicular to the direction of tensile loading (0° and 90°, respectively).

For the validation study, the effective modulus estimated from the meshed FE model was compared to the average experimental elastic modulus of bioplotted specimens (n = 3) of the same porous geometry. The experimental stress versus strain plots and the three tensile measures are presented in Figure 7(a). Stress undulations were observed after the yield point, similar to the trend seen in bulk specimens of 0° configuration. The difference between the FE-estimated and experimental elastic moduli (37.51 N/mm^2 and 34.63 N/mm^2, respectively) was 8.3%. A comparison of experimentally-determined tensile properties of non-porous bulk specimens of 0° and 90° configurations and porous specimens with 1:1 ratio of strand width to inter-strand spacing is presented in Figure 7(b). On average, the tensile properties of the porous specimens were 44% and 13% less than those of 0° and 90° configurations, respectively.

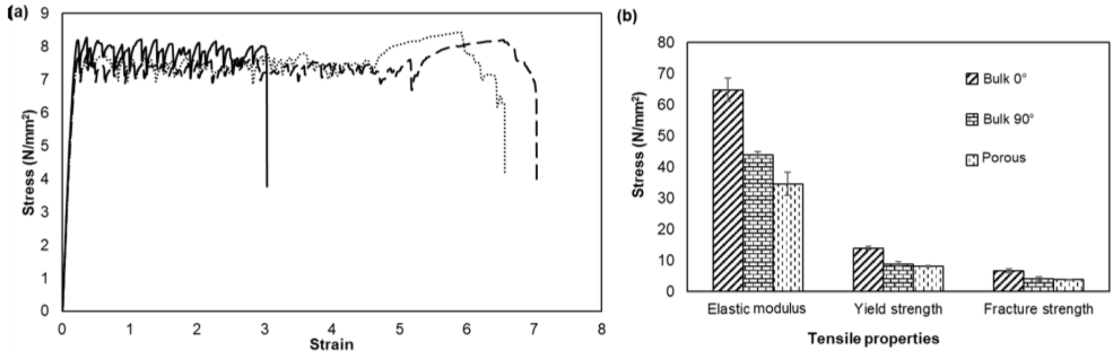

Figure 7. (a) Stress versus strain plots for three porous tensile represented by lines with different types of line style and **(b)** Comparison of experimental tensile properties of bulk and porous specimens. Error bars denote standard deviation (n = 3).

4. Discussion

Assigning optimal levels of process parameters is critical to the micro-architecture and geometric fidelity of bioplotted scaffolds. A previous study had demonstrated how changes in nozzle diameter and extrusion temperature affect the bioplotted PCL strand width [11]. Phase-1 results of this study show that for a given nozzle diameter and extrusion temperature, changes in extrusion pressure and nozzle speed significantly affect the strand width, while the effects of the two geometry-specific factors (lay orientation and strand length) are not significant. The strand width is directly proportional to extrusion pressure. This phenomenon occurs due to the increase in flow rate of the extruded polymer through the nozzle with increasing pressure [17]. On the other hand, the strand width is inversely proportional to the nozzle speed. As the speed increases, there is a decrease in the dispensing time of the polymer per unit length traversed by the nozzle. With the extrusion flow rate remaining constant, this leads to a decrease in the volume of polymer deposited per unit length traversed by the nozzle. This decrease in volume deposited per unit length, in turn, translates to a decrease in strand width [33]. The results from the aB reduction assay confirm that the strand width and corresponding inter-strand spacing, which govern the micro-architecture of the scaffold, play an important role in regulating cellular activity. Whereas the overall size and ratio of strand width to inter-strand spacing were the same in both 3DB1 and 3DB2 scaffold designs (Ø 20 × 2 mm and 1:1, respectively), the smaller bioplotted strand width and corresponding inter-strand spacing resulted in higher effective surface area of 3DB2 (3462.85 mm^2) compared to 3DB1 (2367.61 mm^2), as estimated from their CAD models. Higher cell proliferation observed in 3DB2 can be primarily attributed to the higher surface area available for the adherent cells to attach to and proliferate. This observation is consistent with higher cellular migration and adhesion of pre-osteoblastic murine cells reported in scaffolds having higher effective surface area [34]. As such, having precise control over the strand width through mapping of process parameters can streamline the efforts in designing scaffolds for different tissue engineering applications.

Tensile testing of bulk specimens in Phase-2 was performed in order to create the FE model. Any FE model requires a base line mechanical properties of the materials used in the model. Since, the mechanical properties of solid bioplotted PCL are not reported in literature, the bulk samples of 0° and 90° configurations were fabricated and tensile tested to the determine the appropriate solid 3DB PCL's tensile properties. Table 3 presents a summary of PCL tensile properties reported in literature. Similar to most other polymers, tensile properties of PCL vary with the molecular weight [35,36] and the degree of mechanical compaction due to the pressure applied during primary and secondary processing operations [37,38]. For example, the strength of structures manufactured via injection molding and extrusion is typically greater than that of structures processed using AM [22,29]. Furthermore, mechanical properties of structures fabricated using AM processes such as SLS, FDM, and 3DB are generally anisotropic [19,39–41]. This directional dependency arises, in part, due to poor inter-strand and inter-layer adhesion that occurs as a result of layer-wise processing. At the inter-layer interface, the degree of macromolecular entanglement during recrystallization of the polymer melt is lower, resulting in decreased mechanical strength [42]. The mechanical properties are also affected by the strand lay pattern [19,42]. In the case of FDM and 3DB, the lay pattern is dictated by the strand lay orientation and inter-strand spacing. The lay pattern can affect the mechanical properties due to the differences in effective interfacial area and macromolecular (re)crystallization at the interface between layers. The degree of macromolecular polymer chain re-entanglement within a strand is generally higher than at the inter-layer interface. Ahn et al. have demonstrated how process parameters such as lay orientation, inter-strand spacing, and extrusion temperature affect the tensile strength of FDM-printed ABS structures [19]. Eshraghi and Das have documented the differences in mechanical properties of SLS-printed PCL structures in response to changes in parameters such as lay orientation, inter-strand spacing, and laser power and speed [22]. Domingos et al. have reported on the differences in compression strength of extrusion-plotted PCL scaffolds in response to changes in the strand lay orientation and inter-strand spacing [43].

Table 3. Tensile properties of PCL reported in literature

Reference	**Molecular weight (M_w)**	**Fabrication process**	**Geometry**	**Elastic modulus (N/mm^2)**	**Yield strength (N/mm^2)**
Manufacturer – Perstorp [44]	84,500	Injection molding	*n/a*	430	17.5
Granado et al. [45]	80,000	Injection molding	Sheet	300	14
Engelberg and Kohn [31]	72,500	Compression molding	Sheet	400	16
Pitt et al. [46]	84,500	Melt extrusion	Dumbbell shaped	264.8	*n/a*
Tan et al. [47]	80,000	Electrospinning	Single fiber	120	13
Wong et al. [48]	80,000	Electrospinning	Sheet	237	14
Lee et al. [49]	80,000	Electrospinning	Nonwoven mat	331	56
Eshraghi and Das [22]	73,000	SLS	Bulk - solid gage (0°)	363.4	8.2
Eshraghi and Das [22]	73,000	SLS	Bulk - solid gage (90°)	343.9	10.1
Cahill et al. [50]	*n/a*	SLS	Hollow Strut	47	*n/a*
Manufacturer – Absorbables [51]	75,000	*n/a*	*n/a*	241.3	20.6

Manufacturer - Sigma Aldrich [52]	43,000-80,000	*n/a*	*n/a*	261.4-400	18.6-36.5
Narayanan and Shirwaiker	43,000	3DB (Melt extrusion)	Bulk - solid gage (0°)	63.30 ± 3.64	13.40 ± 0.46
Narayanan and Shirwaiker	43,000	3DB (Melt extrusion)	Bulk - solid gage (90°)	43.89 ± 1.01	8.88 ± 0.67

Similar anisotropic relationships were observed in the tensile properties of bioplotted PCL in Phase-2. The specimens of 0° configuration exhibited higher values for all three tensile measures. In these specimens, the tensile load was borne by the cross-sections of individual strands which were aligned along the direction of loading. On the other hand, in 90° configuration specimens, the tensile load was borne by interfacial area of adjacent strands which were perpendicular to direction of loading. The relative weakness in this interfacial area can be attributed to the nature of the 3DB process wherein molten strands are deposited adjacent to strands that have already solidified completely or partially. Such differences in strength resulting from variations in strand lay orientation can be utilized to additively manufacture scaffolds for tissues that require anisotropy. The 44% reduction in elastic modulus of porous specimen compared to bulk 0° configuration in bioplotted PCL was a similar in trend as reported in SLS-printed PCL (40%) [22].

The inherent nature of the manufacturing process along with the actual processing parameters affect the strand geometry and inter-strand spacing, which in turn, govern scaffolds' porous micro-architecture and mechanical properties. To satisfy their physiological functional requirements, scaffolds must possess high porosity to facilitate nutrient and gas exchange as well mechanical properties that match those of the native tissue. Mechanical properties are especially important for load bearing tissues such as bone and cartilage which experience complex loading conditions. The forces that these tissues experience may act in multiple directions coupled with rotational components and can also be cyclic in nature. Determining appropriate scaffold micro-architecture to achieve desired mechanical characteristics using purely experimental testing can be time consuming and expensive. Additionally, some applications may require the use of robotic testing systems to simulate the complex loading conditions. One alternative strategy is to assess scaffold designs and resulting mechanical characteristics computationally using FE analysis. Once the appropriate FE model is developed, design features including strand geometry and inter-strand spacing can be altered and the simulations run until the required properties are achieved. However, it is also necessary to experimentally validate the accuracy of the model and confirm its fidelity.

Phase-3 validation results showed that the FE-estimated effective elastic modulus of bioplotted PCL was in good agreement with the experimentally-determined elastic modulus (difference of 8.3%). Much higher differences between computational and experimental moduli have been reported for SLS-printed scaffolds [22,29,50,53]. For instance, Williams et al. noted that their FE moduli estimates were 50% lower than the experimental compressive moduli of SLS-printed bulk PCL scaffolds [29]. Conversely, Cahill et al. and Eshraghi and Das reported higher FE-estimated moduli (67% and 30%, respectively) of SLS-fabricated porous PCL scaffolds. Both those studies attributed the observed differences to the packing density of the SLS powder bed and micro-defects in the fabricated structures. Melt extrusion-based 3DB offers a more uniform control over the strand micro-structure in comparison to powder-based fabrication processes such as SLS, which may have resulted in better FE model fidelity [54,55]. In future, the fidelity of the 3DB FE-model can be further improved by more accurately capturing the input geometry (e.g., micro-computed tomography (μCT) imaging analysis) and using experimentally-determined Poisson's ratio.

5. Conclusions

This study models important process-structures relationships in the bioplotting of PCL. Critical 3DB parameters (extrusion pressure and nozzle speed) were mapped to the bioplotted strand width, and a least square regression model was developed and validated to estimate the strand width for a given set of process parameters. Evaluation of two scaffold designs of the same overall size but with different bioplotted strand widths under the same cell culture conditions highlighted differences in cellular activity. The scaffold design with the smaller strand width and corresponding inter-strand spacing, which had a higher effective surface area to facilitate attachment of adherent NIH/3T3 cells, demonstrated higher proliferation over the first 5 days in culture. In addition, strand lay orientation was determined to significantly affect the tensile properties (elastic modulus, yield strength, fracture strength) of bioplotted PCL. This is in agreement with the AM theory wherein strand-based layer-by-layer approach and resulting adhesion characteristics affect the mechanical properties of printed structures. A FE model was also was developed and validated to estimate the effective elastic modulus and stress distribution in bioplotted porous PCL. The FE-estimated effective elastic modulus was comparable to the experimental elastic modulus, and as such, the fidelity of this FE model is better than that reported for FE models of SLS-printed PCL.

Micro-architecture and mechanical properties are important parameters in the design of scaffolds for tissue engineering. The least square regression and FE models developed in this study provide an efficient alternative to the experimental characterization of the design and mechanical properties of scaffolds. For example, based on the results of the FE model, users can determine appropriate strand width and inter-strand spacing that would allow the scaffold to satisfy the application specific tensile strength requirements. The regression model can then be used to estimate the 3DB process parameters to produce scaffolds with the desired strand width. In addition to the models, the methods used in this study can be applied to characterize process-structure interactions of other additively manufactured polymers.

Author Contributions: R.A.S and LKN were both responsible for the conceptualization, methodology used in investigation, data curation and writing of research presented in this paper.

Funding: This research received no external funding.

Acknowledgments: The authors would like to thank Dr. Harvey West (North Carolina State University, Industrial and Systems Engineering Department) for help with the tensile testing experiments.

Conflicts of Interest: The authors declare no conflict of interest.

References

1. Lanza, R.P. (Robert P.; Langer, R.S.; Vacanti, J. *Principles of tissue engineering*; Elsevier Academic Press, 2007; ISBN 9780080548845.
2. Fisher, J.P.; Mikos, A.G.; Bronzino, J.D. *Tissue engineering*; CRC Press/Taylor & Francis Group: Milton Park, UK, 2007; ISBN 9780849390265.
3. O'Brien, F.J. Biomaterials & scaffolds for tissue engineering. *Mater. Today* **2011**, *14*, 88–95, doi:http://dx.doi.org/10.1016/S1369-7021(11)70058-X.
4. Jafari, M.; Paknejad, Z.; Rad, M.R.; Motamedian, S.R.; Eghbal, M.J.; Nadjmi, N.; Khojasteh, A. Polymeric scaffolds in tissue engineering: a literature review. *J. Biomed. Mater. Res. Part B Appl. Biomater.* **2017**, *105*, 431–459, doi:10.1002/jbm.b.33547.
5. Duan, B.; Wang, M.; Zhou, W.Y.; Cheung, W.L.; Li, Z.Y.; Lu, W.W. Three-dimensional nanocomposite scaffolds fabricated via selective laser sintering for bone tissue engineering. *Acta Biomater.* **2010**, *6*, 4495–4505, doi:10.1016/j.actbio.2010.06.024.
6. Tan, K..; Chua, C..; Leong, K..; Cheah, C..; Cheang, P.; Abu Bakar, M..; Cha, S.. Scaffold development

using selective laser sintering of polyetheretherketone–hydroxyapatite biocomposite blends. *Biomaterials* **2003**, *24*, 3115–3123, doi:10.1016/S0142-9612(03)00131-5.

7. Yen, H.-J.; Tseng, C.-S.; Hsu, S.; Tsai, C.-L. Evaluation of chondrocyte growth in the highly porous scaffolds made by fused deposition manufacturing (FDM) filled with type II collagen. *Biomed. Microdevices* **2009**, *11*, 615–624, doi:10.1007/s10544-008-9271-7.
8. Zein, I.; Hutmacher, D.W.; Tan, K.C.; Teoh, S.H. Fused deposition modeling of novel scaffold architectures for tissue engineering applications. *Biomaterials* **2002**, *23*, 1169–1185, doi:10.1016/S0142-9612(01)00232-0.
9. Carvalho, C.; Landers, R.; Hübner, U.; Schmelzeisen, R.; Mülhaupt, R. Fabrication of soft and hard biocompatible scaffolds using 3D-Bioplotting. *Virtual Model. Rapid Manuf. Res. Virtual Rapid Prototyping. London, Engl. Taylor Fr. Gr.* **2005**, 97–102.
10. Narayanan, L.K.; Huebner, P.; Fisher, M.B.; Spang, J.T.; Starly, B.; Shirwaiker, R.A. 3D-Bioprinting of Polylactic Acid (PLA) Nanofiber–Alginate Hydrogel Bioink Containing Human Adipose-Derived Stem Cells. *ACS Biomater. Sci. Eng.* **2016**, *2*, 1732–1742, doi:10.1021/acsbiomaterials.6b00196.
11. Sheshadri, P.; Shirwaiker, R.A. Characterization of Material – Process – Structure Interactions in the 3D Bioplotting of Polycaprolactone., doi:10.1089/3dp.2014.0025.
12. Cooke, M.N.; Fisher, J.P.; Dean, D.; Rimnac, C.; Mikos, A.G. Use of stereolithography to manufacture critical-sized 3D biodegradable scaffolds for bone ingrowth. *J. Biomed. Mater. Res.* **2003**, *64B*, 65–69, doi:10.1002/jbm.b.10485.
13. Elomaa, L.; Teixeira, S.; Hakala, R.; Korhonen, H.; Grijpma, D.W.; Seppälä, J. V. Preparation of poly(ε-caprolactone)-based tissue engineering scaffolds by stereolithography. *Acta Biomater.* **2011**, *7*, 3850–3856, doi:10.1016/j.actbio.2011.06.039.
14. Gómez-Lizárraga, K.K.; Flores-Morales, C.; Del Prado-Audelo, M.L.; Álvarez-Pérez, M.A.; Piña-Barba, M.C.; Escobedo, C. Polycaprolactone- and polycaprolactone/ceramic-based 3D-bioplotted porous scaffolds for bone regeneration: A comparative study. *Mater. Sci. Eng. C* **2017**, *79*, 326–335, doi:10.1016/j.msec.2017.05.003.
15. Naghieh, S.; Sarker, M.; Karamooz-Ravari, M.; McInnes, A.; Chen, X. Modeling of the Mechanical Behavior of 3D Bioplotted Scaffolds Considering the Penetration in Interlocked Strands. *Appl. Sci.* **2018**, *8*, 1422, doi:10.3390/app8091422.
16. Leferink, A.M.; Hendrikson, W.J.; Rouwkema, J.; Karperien, M.; van Blitterswijk, C.A.; Moroni, L. Increased cell seeding efficiency in bioplotted three-dimensional PEOT/PBT scaffolds. *J. Tissue Eng. Regen. Med.* **2016**, *10*, 679–689, doi:10.1002/term.1842.
17. Ramanath, H.S.; Chua, C.K.; Leong, K.F.; Shah, K.D. Melt flow behaviour of poly-epsilon-caprolactone in fused deposition modelling. *J. Mater. Sci. Mater. Med.* **2008**, *19*, 2541–50, doi:10.1007/s10856-007-3203-6.
18. Vozzi, G.; Corallo, C.; Daraio, C. Pressure-activated microsyringe composite scaffold of poly(L -lactic acid) and carbon nanotubes for bone tissue engineering. *J. Appl. Polym. Sci.* **2013**, *129*, 528–536, doi:10.1002/app.38235.
19. Ahn, S.; Montero, M.; Odell, D.; Roundy, S.; Wright, P.K. Anisotropic material properties of fused deposition modeling ABS. *Rapid Prototyp. J.* **2002**, *8*, 248–257, doi:10.1108/13552540210441166.

20. Anitha, R.; Arunachalam, S.; Radhakrishnan, P. Critical parameters influencing the quality of prototypes in fused deposition modelling. *PART 1 Contain. Pap. Present. Int. Conf. Adv. Mater. Process. Technol.* **2001**, *118*, 385–388, doi:http://dx.doi.org/10.1016/S0924-0136(01)00980-3.
21. Górski, F.; Kuczko, W.; Wichniarek, R. Influence of process parameters on dimensional accuracy of parts manufactured using Fused Deposition Modelling technology. *Adv. Sci. Technol. Res. J.* **2013**, *7*, 27–35.
22. Eshraghi, S.; Das, S. Mechanical and microstructural properties of polycaprolactone scaffolds with one-dimensional, two-dimensional, and three-dimensional orthogonally oriented porous architectures produced by selective laser sintering. *Acta Biomater.* **2010**, *6*, 2467–76, doi:10.1016/j.actbio.2010.02.002.
23. Liu, F.; Vyas, C.; Poologasundarampillai, G.; Pape, I.; Hinduja, S.; Mirihanage, W.; Bartolo, P.J. Process-Driven Microstructure Control in Melt-Extrusion-Based 3D Printing for Tailorable Mechanical Properties in a Polycaprolactone Filament. *Macromol. Mater. Eng.* **2018**, 1800173, doi:10.1002/mame.201800173.
24. Gleadall, A.; Visscher, D.; Yang, J.; Thomas, D.; Segal, J. Review of additive manufactured tissue engineering scaffolds: relationship between geometry and performance. *Burn. Trauma* **2018**, *6*, doi:10.1186/s41038-018-0121-4.
25. Narayanan, L.K.; Kumar, A.; Tan, Z. (George); Bernacki, S.; Starly, B.; Shirwaiker, R.A. Alginate Microspheroid Encapsulation and Delivery of MG-63 Cells Into Polycaprolactone Scaffolds: A New Biofabrication Approach for Tissue Engineering Constructs. *J. Nanotechnol. Eng. Med.* **2015**, *6*, 021003-021003–8, doi:10.1115/1.4031174.
26. ASTM Standard Test Method for Tensile Properties of Plastics Available online: https://www.astm.org/Standards/D638.htm (accessed on Aug 14, 2018).
27. Bañobre-López, M.; Piñeiro-Redondo, Y.; De Santis, R.; Gloria, A.; Ambrosio, L.; Tampieri, A.; Dediu, V.; Rivas, J. Poly(caprolactone) based magnetic scaffolds for bone tissue engineering. *J. Appl. Phys.* **2011**, *109*, 07B313, doi:10.1063/1.3561149.
28. Park, S.A.; Lee, S.H.; Kim, W.D. Fabrication of porous polycaprolactone/hydroxyapatite (PCL/HA) blend scaffolds using a 3D plotting system for bone tissue engineering. *Bioprocess Biosyst. Eng.* **2011**, *34*, 505–513, doi:10.1007/s00449-010-0499-2.
29. Williams, J.M.; Adewunmi, A.; Schek, R.M.; Flanagan, C.L.; Krebsbach, P.H.; Feinberg, S.E.; Hollister, S.J.; Das, S. Bone tissue engineering using polycaprolactone scaffolds fabricated via selective laser sintering. *Biomaterials* **2005**, *26*, 4817–4827, doi:10.1016/j.biomaterials.2004.11.057.
30. Baji, A.; Mai, Y.-W.; Wong, S.-C.; Abtahi, M.; Chen, P. Electrospinning of polymer nanofibers: Effects on oriented morphology, structures and tensile properties. *Compos. Sci. Technol.* **2010**, *70*, 703–718, doi:10.1016/J.COMPSCITECH.2010.01.010.
31. Engelberg, I.; Kohn, J. Physico-mechanical properties of degradable polymers used in medical applications: A comparative study. *Biomaterials* **1991**, *12*, 292–304, doi:10.1016/0142-9612(91)90037-B.
32. Abu Bakar, M.S.; Cheng, M.H.W.; Tang, S.M.; Yu, S.C.; Liao, K.; Tan, C.T.; Khor, K.A.; Cheang, P. Tensile properties, tension–tension fatigue and biological response of polyetheretherketone–hydroxyapatite composites for load-bearing orthopedic implants. *Biomaterials* **2003**, *24*, 2245–2250, doi:10.1016/S0142-9612(03)00028-0.
33. Pfister, A.; Landers, R.; Laib, A.; Hübner, U.; Schmelzeisen, R.; Mülhaupt, R. Biofunctional rapid

prototyping for tissue-engineering applications: 3D bioplotting versus 3D printing. *J. Polym. Sci. Part A Polym. Chem.* **2004**, *42*, 624–638, doi:10.1002/pola.10807.

34. Murphy, C.M.; Haugh, M.G.; O'Brien, F.J. The effect of mean pore size on cell attachment, proliferation and migration in collagen–glycosaminoglycan scaffolds for bone tissue engineering. *Biomaterials* **2010**, *31*, 461–466, doi:10.1016/j.biomaterials.2009.09.063.
35. Van De Velde, K.; Kiekens, P. Biopolymers: overview of several properties and consequences on their applications. *Polym. Test.* **2002**, *21*, 433–442.
36. Södergård, A.; Stolt, M. Properties of lactic acid based polymers and their correlation with composition. *Prog. Polym. Sci.* **2002**, *27*, 1123–1163, doi:10.1016/S0079-6700(02)00012-6.
37. Hussain, F.; Hojjati, M.; Okamoto, M.; Gorga, R.E. Review article: Polymer-matrix Nanocomposites, Processing, Manufacturing, and Application: An Overview. *J. Compos. Mater.* **2006**, *40*, 1511–1575, doi:10.1177/0021998306067321.
38. Ku, H.; Wang, H.; Pattarachaiyakoop, N.; Trada, M. A review on the tensile properties of natural fiber reinforced polymer composites. *Compos. Part B Eng.* **2011**, *42*, 856–873, doi:10.1016/j.compositesb.2011.01.010.
39. Lee, C.S.; Kim, S.G.; Kim, H.J.; Ahn, S.H. Measurement of anisotropic compressive strength of rapid prototyping parts. *J. Mater. Process. Technol.* **2007**, *187*, 627–630, doi:10.1016/j.jmatprotec.2006.11.095.
40. Butscher, A.; Bohner, M.; Hofmann, S.; Gauckler, L.; Müller, R. Structural and material approaches to bone tissue engineering in powder-based three-dimensional printing. *Acta Biomater.* **2011**, *7*, 907–920, doi:10.1016/j.actbio.2010.09.039.
41. Inzana, J.A.; Olvera, D.; Fuller, S.M.; Kelly, J.P.; Graeve, O.A.; Schwarz, E.M.; Kates, S.L.; Awad, H.A. 3D printing of composite calcium phosphate and collagen scaffolds for bone regeneration. *Biomaterials* **2014**, *35*, 4026–4034, doi:10.1016/j.biomaterials.2014.01.064.
42. Bellini, A.; Güçeri, S. Mechanical characterization of parts fabricated using fused deposition modeling. *Rapid Prototyp. J.* **2003**, *9*, 252–264, doi:10.1108/13552540310489631.
43. Domingos, M.; Intranuovo, F.; Russo, T.; Santis, R. De; Gloria, A.; Ambrosio, L.; Ciurana, J.; Bartolo, P. The first systematic analysis of 3D rapid prototyped poly(ε-caprolactone) scaffolds manufactured through BioCell printing: the effect of pore size and geometry on compressive mechanical behaviour and *in vitro* hMSC viability. *Biofabrication* **2013**, *5*, 045004, doi:10.1088/1758-5082/5/4/045004.
44. Biopolymers- Perstorp Available online: https://www.perstorp.com/en/products/plastic_materials/bioplastics/biopolymers.
45. Granado, A.; Eguiazábal, J.I.; Nazábal, J. Structure and mechanical properties of blends of poly(ε-caprolactone) with a poly(amino ether). *J. Appl. Polym. Sci.* **2008**, *109*, 3892–3899, doi:10.1002/app.28615.
46. Pitt, C.G.; Gratzl, M.M.; Kimmel, G.L.; Surles, J.; Schindler, A. Aliphatic polyesters II. The degradation of poly (DL-lactide), poly (epsilon-caprolactone), and their copolymers in vivo. *Biomaterials* **1981**, *2*, 215–20.
47. Tan, E.P.S.; Ng, S.Y.; Lim, C.T. Tensile testing of a single ultrafine polymeric fiber. *Biomaterials* **2005**, *26*, 1453–1456, doi:10.1016/j.biomaterials.2004.05.021.
48. Wong, S.-C.; Baji, A.; Leng, S. Effect of fiber diameter on tensile properties of electrospun poly(ε-caprolactone). *Polymer (Guildf).* **2008**, *49*, 4713–4722, doi:10.1016/j.polymer.2008.08.022.

49. Lee, K.H.; Kim, H.Y.; Khil, M.S.; Ra, Y.M.; Lee, D.R. Characterization of nano-structured poly(ε-caprolactone) nonwoven mats via electrospinning. *Polymer (Guildf).* **2003**, *44*, 1287–1294, doi:10.1016/S0032-3861(02)00820-0.
50. Cahill, S.; Lohfeld, S.; McHugh, P.E. Finite element predictions compared to experimental results for the effective modulus of bone tissue engineering scaffolds fabricated by selective laser sintering. *J. Mater. Sci. Mater. Med.* **2009**, *20*, 1255–1262, doi:10.1007/s10856-009-3693-5.
51. Chemical & Physical Properties of Select Polymers - LACTEL Absorbable Polymers Available online: http://www.absorbables.com/technical/properties.html (accessed on Aug 13, 2018).
52. Polycaprolactone | Sigma-Aldrich Available online: http://www.sigmaaldrich.com/catalog/product/sial/81277?lang=en&region=US.
53. Luxner, M.H.; Stampfl, J.; Pettermann, H.E. Finite element modeling concepts and linear analyses of 3D regular open cell structures. *J. Mater. Sci.* **2005**, *40*, 5859–5866, doi:10.1007/s10853-005-5020-y.
54. Kim, G.D.; Oh, Y.T. A benchmark study on rapid prototyping processes and machines: Quantitative comparisons of mechanical properties, accuracy, roughness, speed, and material cost. *Proc. Inst. Mech. Eng. Part B J. Eng. Manuf.* **2008**, *222*, 201–215, doi:10.1243/09544054JEM724.
55. Griffin, E.A.; Mcmillin, S. Selective Laser Sintering and Fused Deposition Modeling Processes For Functional Ceramic Parts. In Proceedings of the Solid Freeform Fabrication (SFF) Symposium; Austin, Texas, 1995; pp. 25–30.